

Particle modeling of dynamic fragmentation—II: Fracture in single- and multi-phase materials

G. Wang^a, M. Ostoja-Starzewski^{a,*}, P. Radziszewski^a, M. Ourriban^b

^a Department of Mechanical Engineering, McGill University, 817 Sherbrooke Street West, Montreal, Qué., Canada H3A 2K6

^b Consortium de Recherche Minérale (COREM), Québec City, Qué., Canada G1N 1X7

Received 10 December 2004; received in revised form 3 March 2005; accepted 17 March 2005

Abstract

The second paper of this series adopts particle modeling (PM) to simulation of dynamic fracture phenomena in homogeneous and heterogeneous materials, such as encountered in comminution and blasting processes in mining industry. As the basis for such simulations, we first develop a new method to prevent particles from topologically interpenetrating themselves within the material domain, when actual fracture does not actually take place. We then move to a number of application studies: (i) fragmentation of 2-D single- and multi-phase materials—including a simulation of a drop-weight test—and (ii) fragmentation of 3-D single-phase materials under either very rapid extension or compression. These investigations show patterns and trends of fragmentation of materials in function of their constitutive properties, their geometric shapes, and the loading conditions.

© 2005 Elsevier B.V. All rights reserved.

PACS: 68.45.Kg; 61.43.Bn; 62.50.+p; 46.30.My; 46.30.Nz; 83.80.Nb; 83.20.-d

Keywords: Dynamics; Structural modeling; Shocks; Fracture mechanics; Cracks; Minerals; Constitutive relations; Comminution

1. Introduction

The paper series is concerned with particle modeling (PM) as a simulation tool of dynamic fracture phenomena in homogeneous and heterogeneous materials. This first part of the series [1] was concerned with the setup of a lattice-type particle model having the same functional form as the molecular dynamics (MD) model (i.e., the Lennard–Jones potential), yet on centimeter length scales. In [1] we formulated four conditions to determine four key parameters of the PM model—functionally also of the Lennard–Jones type—from a given MD model. This led to a number of properties and trends of resulting Young's modulus in function of these

four parameters. As an application, we studied dynamic fragmentation of a copper plate with a skew slit.

The particle modeling—also called *particle simulation*, *discrete modeling* or *quasi-molecular modeling* [2–5]—is a dynamic simulation method that typically uses a lattice of small (but not molecular level) particles, evolving according to laws of mechanics, as a discrete representation of fluids and/or solids. The method is set up so as to maintain the conservation of mass and energy of the particle system and satisfy the interaction laws between all the particles. As demonstrated in the above cited references, the PM can handle a wide range of complex material systems, problems with complicated boundary shapes and boundary conditions, dynamic free surfaces, and fracture of solids. Our work continues such multifarious applications.

In the first paper [1], we developed this method to the stage of potentially real applications in that, we

* Corresponding author. Tel.: +1 514 3987394; fax: +1 514 3987365.
E-mail address: martin.ostoja@mcgill.ca (M. Ostoja-Starzewski).

¹ Also with McGill Institute for Advanced Materials.

formulated four conditions to determine continuum-level Young's modulus and tensile strength in the PM model from a given MD model. We then broadened the range of Greenspan's modeling from "particle interaction being small relative to gravity" to one allowing a fully dynamic solution. This involved a new stability criterion for determining time increments. Furthermore, we carried out a quite detailed study of how the material properties, are affected by: (i) different choices of the power exponents in the (p, q) pair which figure in the interaction force equation; (ii) the size of a simulated domain of material; (iii) the equilibrium spacing r_0 between quasi-particles; (iv) the combined changes in all these aspects. Our investigation demonstrated how these different choices directly affected the Young's modulus and strength of material, as well as its transition from a brittle to a ductile type. We found that it was possible to produce a required Young's modulus by not only changing (p, q) , but also by choosing a simu-

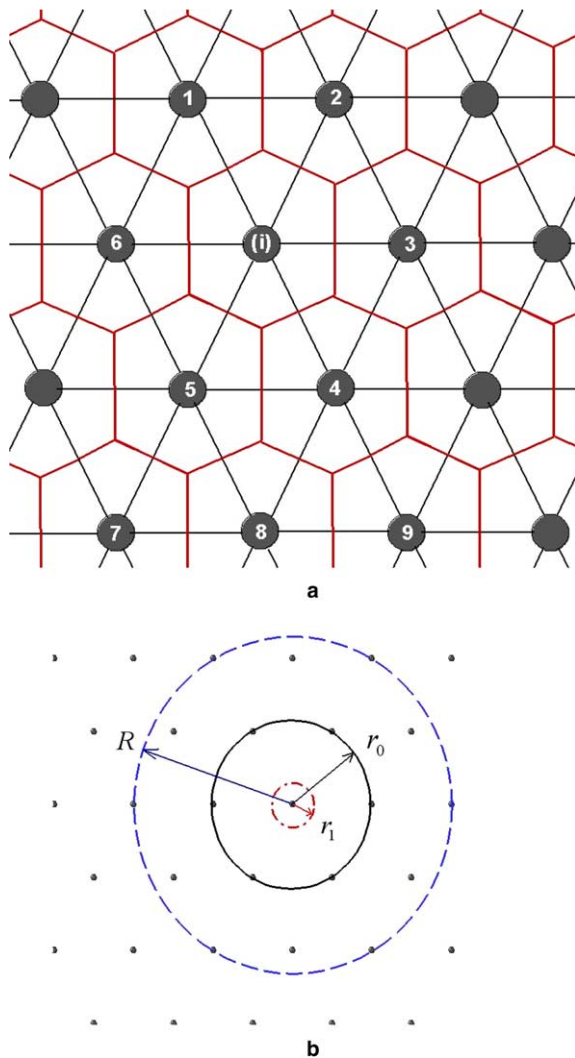


Fig. 1. Particle concept in PM: (a) discretization of a solid material into quasi-particles and (b) neighborhood of particle i in PM.

lated domain based on a certain equilibrium spacing of mutually interacting quasi-particles.

In this second part of paper series we focus on dynamic fragmentation of minerals such as encountered in comminution and blasting processes in the mining industry. In particular, we simulate single as well as multi-phase materials in two dimensions (2-D) and 3-D that are stretched or compressed, and then fractured/crushed at a wide range of kinetic/dynamic loading conditions. As argued in [6], different time increments are adopted for stretching and compression. We choose equilibrium spacing between contiguous particles to be $r_0 = 0.2$ cm.

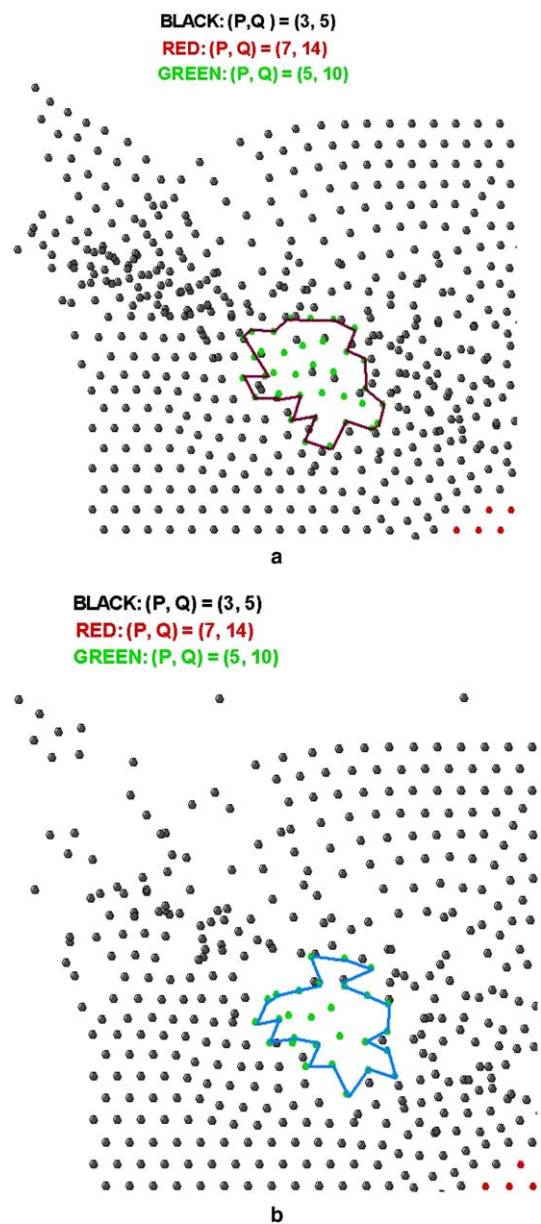


Fig. 2. The lattice interpenetration problem and its solution in PM: (a) interpenetration takes place and (b) no interpenetration takes place.

2. Handling the lattice interpenetration problem in PM

An important challenge, and one that is hardly mentioned and/or discussed in the PM studies, is the possibility of local interpenetration of a lattice of particles. In the language of continuum mechanics, this would signify the violation of the strain compatibility condition. In principle, due to its long tail of the interaction potential, each and every particle interacts with $N-1$ other particles. However, since an exact solution to the N -body problem is prohibitively expensive, it is commonly recommended [4,7] that each particle reacts only with its nearest neighbors defined by the equilibrium spacing r_0 , but not with further neighbors. Thus, with respect to the lattice shown in Fig. 1(a), particle i interacts with particles 1, 2, ..., 6. Under slow to moderate strain rates, and over short times, this approach is reasonable. How-

ever, under dynamic loading conditions, it is likely to lead to topologically unrealistic (and unacceptable) interpenetration of particles that were not neighbors on the original (undeformed) lattice—we call it a *lattice interpenetration problem*.

Fig. 2(a) illustrates this problem on the example of impact of a matrix–inclusion composite of studied in full detail in Fig. 10 under loading shown in Fig. 11. Here we focus on the top-left corner at the instant $T = 1.6 \times 10^{-5}$ s, whereby only the nearest neighborhood is considered. Clearly, it is seen that some black particles representing the matrix, penetrate into the region of green particles representing an inclusion. Since each particle represents a certain portion of the material body—not an actual molecule as in MD—it is unrealistic if it happens to penetrate through the other particles when actual fracture does not yet take place. We note here

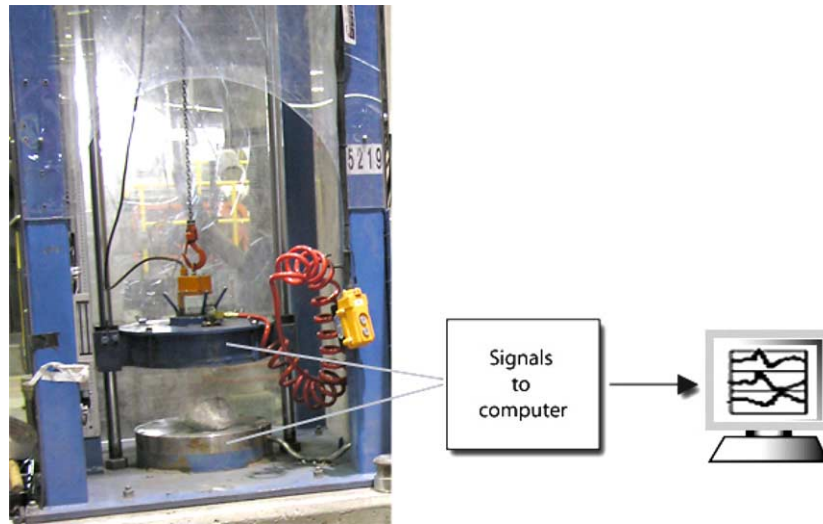


Fig. 3. Drop-weight test.

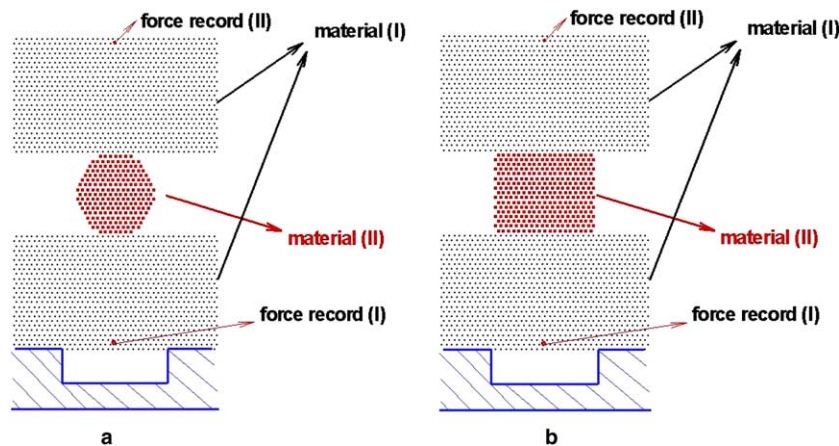


Fig. 4. Model of the drop-weight test of Fig. 3. Material (I): $(p, q) = (7, 14)$; material (II): $(p, q) = (3, 5)$; $(p, q) = (2, 10)$ for two materials: (a) hexagonal and (b) rectangular soft material. Two points are used for force recording.

that both the MD and the PM adopt the same concept that particles only react with each other within their bonding (or truncation) distance [7].

Actually, particles change their positions rather unexpectedly under rapid loading. Thus, in order for the PM to solve the dynamic fragmentation problems properly, an improvement must be made so that not only the nearest, but also further neighbors, are considered when resolving the lattice interpenetration problem. With reference to Fig. 1(b), this is done as follows:

- (i) we define a certain domain outside the nearest neighbor of any given particle and all the particles

within this region, $(r_0, R]$ are its second-nearest neighbors;

- (ii) each particle interacts not only with its nearest neighbors, but also with its second-neighbors providing they come within the distance $r_1 \leq r_0$, shown by a red circle.

Obviously, second-neighbors produce a resistive force to prevent the lattice interpenetration problem and the key question is: “How to choose appropriate R and r_1 then?” Here we observe that choosing a large R means that more second-nearest neighbors are contained, while a small r_1 means that the distance within which they

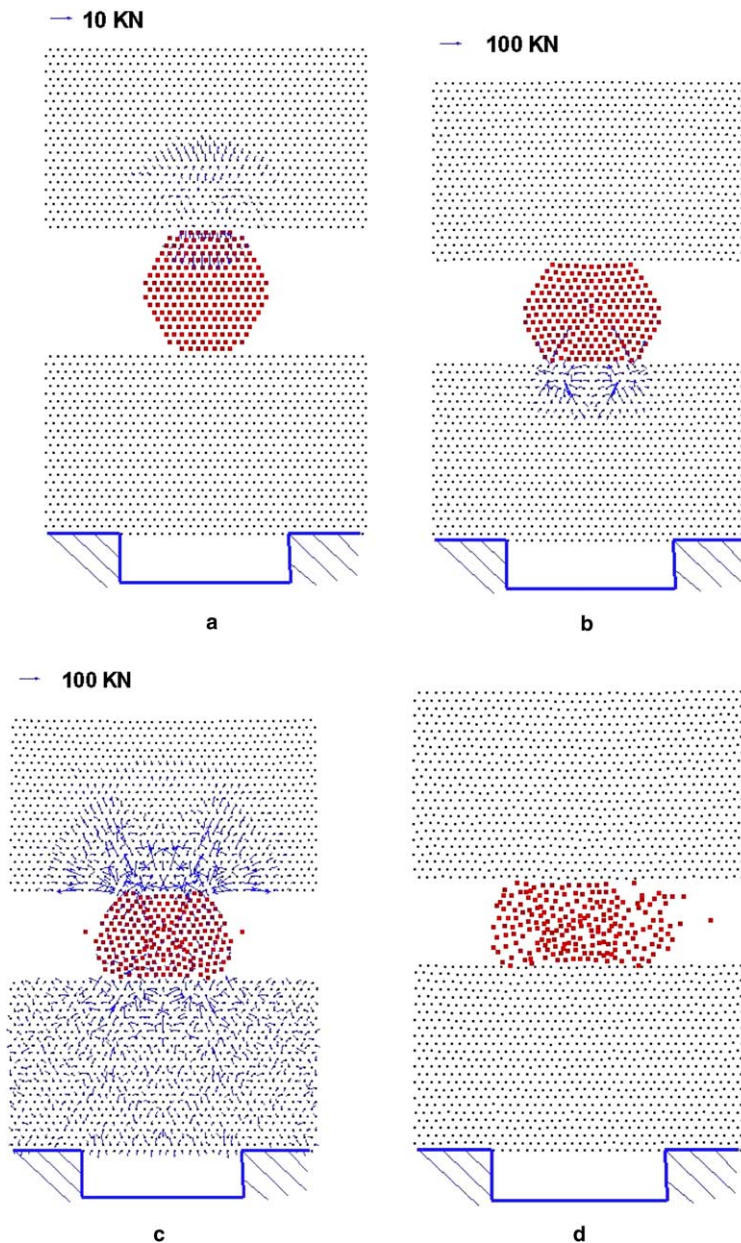


Fig. 5. Time-dependent results for the top dropping at 200 m/s onto the hexagonal specimen: (a) $T = 4.0 \times 10^{-6}$ s; (b) $T = 3.6 \times 10^{-5}$ s; (c) $T = 4.2 \times 10^{-5}$ s; (d) $T = 7.2 \times 10^{-5}$ s.

react with their central particle is small. In conclusion, R depends mainly upon the loading condition while r_1 upon the material property. Thus, we formulate these guidelines:

- if the load is of high magnitude and/or relatively long lasting, then we choose large R ;
- if there exist defects within the material, adopting a large R will avoid figuring out a special solution for interaction of the particle mass with these defects;
- if the material is ductile, a smaller r_1 should be used.

Fig. 2(b) is the result of simulation with the new method, and under the same loading condition as in

Fig. 2(a), whereby we choose $R = 10r_0$ and $r_1 = 0.1r_0$. It is seen that the lattice interpenetration problem is resolved in Fig. 2(b).

3. Application studies by PM

3.1. Fragmentation of 2-D multi-phase material body

3.1.1. Simulation of a drop-weight test

In mineral processing industries, the *drop-weight test* (Fig. 3) is the basic experiment to analyze the ore comminution. As is well known, the top plate drops down so fast, it is practically impossible to follow all the details of

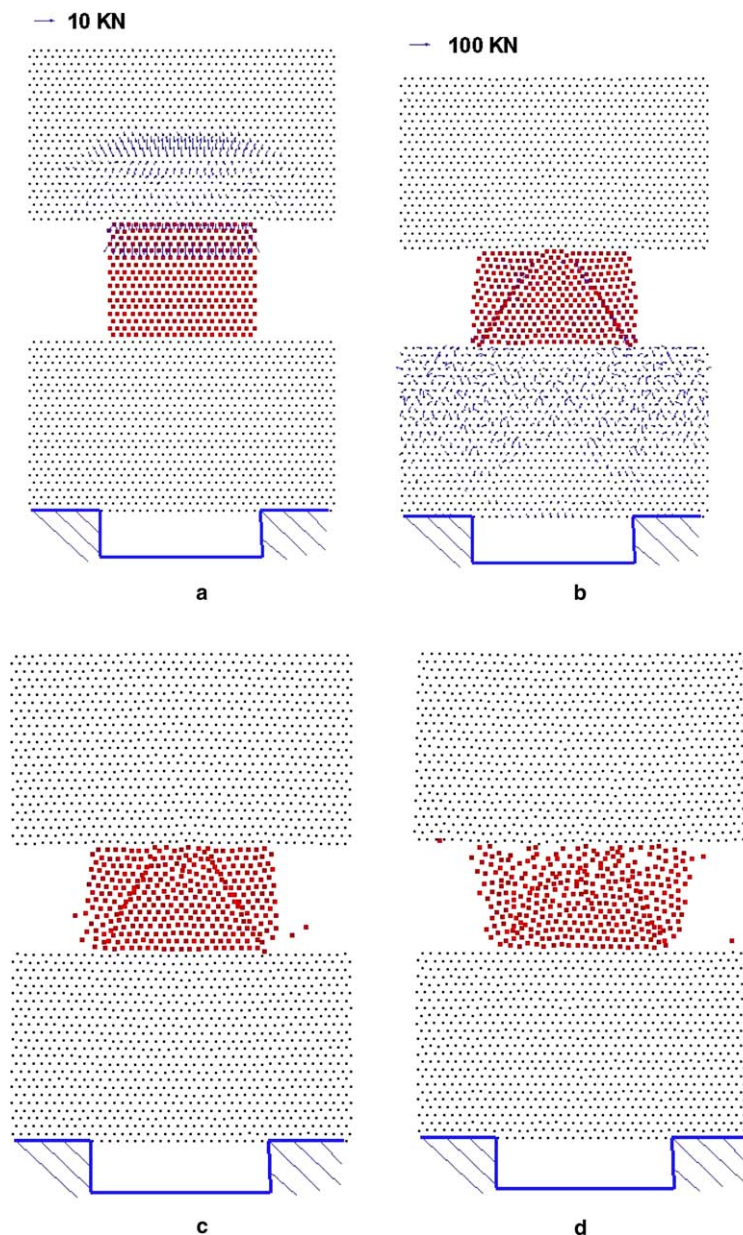


Fig. 6. Time-dependent results for the top dropping at 200 m/s onto the rectangular specimen: (a) $T = 4.0 \times 10^{-6}$ s; (b) $T = 4.2 \times 10^{-5}$ s; (c) $T = 6.4 \times 10^{-5}$ s; (d) $T = 8.4 \times 10^{-5}$ s.

the fragmentation process—a high-speed movie can only provide partial information. Clearly, computational materials science in the form of PM offers a powerful route to study this phenomenon [8].

To simulate the experiment in Fig. 3, we realize the whole process in that, a harder material (I), modeling the top and bottom steel plates, is used to crush the softer one: material (II) is softer and models the ore. Here the latter one is taken in the shape of either (a) hexagon or (b) rectangular block. For the sake of testing this model, we assign, $(p, q) = (7, 14)$ for material (I) and $(p, q) = (3, 5)$ for material (II). The density of material (I) is the same as that of material (II); gravity effects are ignored. To characterize the interaction of both materials at the top and bottom interfaces, we choose $(p, q) = (2, 10)$. Two points near the top and bottom are chosen to record the force histories. Fig. 4(a) and (b) illustrate this simulation set-up. In the following, u and v stand for velocities in the horizontal and vertical directions.

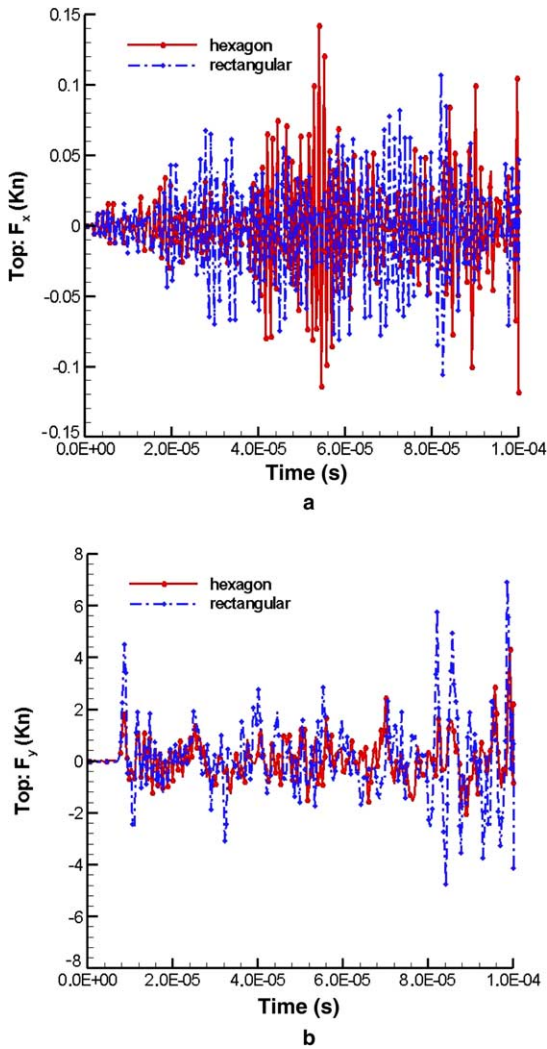


Fig. 7. Time history of the force recorded at the top right-middle point in Fig. 6: (a) F_x and (b) F_y .

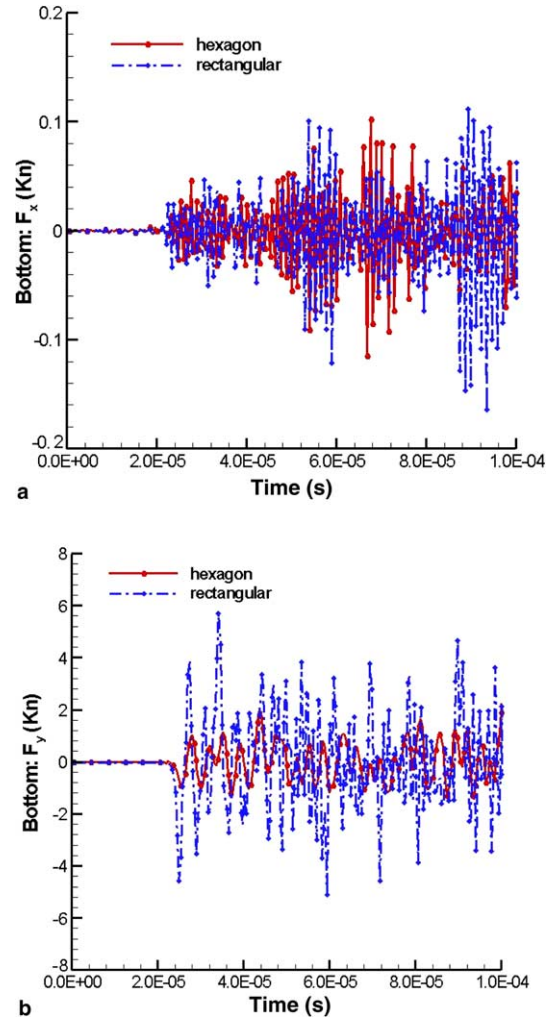


Fig. 8. Time history of the force recorded at the bottom right-middle point in Fig. 6: (a) F_x and (b) F_y .

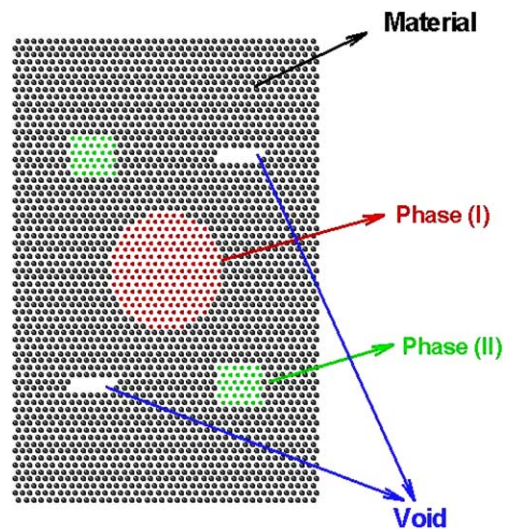


Fig. 9. A composite material specimen with inclusions within: matrix–matrix: $(p, q) = (7, 14)$; phase (I)–phase(I): $(p, q) = (3, 5)$; phase (II)–phase (II): $(p, q) = (5, 10)$; matrix–phase (I): $(p, q) = (2, 10)$; matrix–phase (II): $(p, q) = (2, 10)$; phase (I)–phase (II): $(p, q) = (2, 10)$.

Initial conditions: The top drops down at $v = -200.0$ m/s; $u = v = 0.0$ m/s for the rest of particles at $T = 0.0$ s. The time increment ΔT is determined by the method discussed in [1].

Boundary conditions: $u = v = 0.0$ m/s for the 1/4 particles both from left and right ends of the bottom-line. Traction-free conditions are set on the remaining boundaries.

Figs. 5(a)–(d) and 6(a)–(d), respectively, display the time-dependent results of this process in the case when the comminuted specimen (II) is in the shape of a hexagon or a rectangle. In particular, Figs. 5(a) and 6(a) show how the vector force is distributed at $T = 4.0 \times 10^{-6}$ s just after the specimen has undergone the impact at the top. As that time interval is very short, we see that the reaction force due to the impact at the two material interfaces is transmitted within a small region into these two media. There is no visible change within material (II) at this moment.

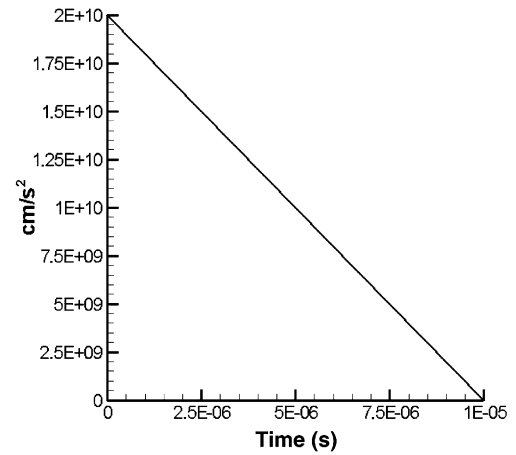


Fig. 10. Time-dependent impact acceleration as a boundary-initial condition applied to the composite material in Fig. 11.

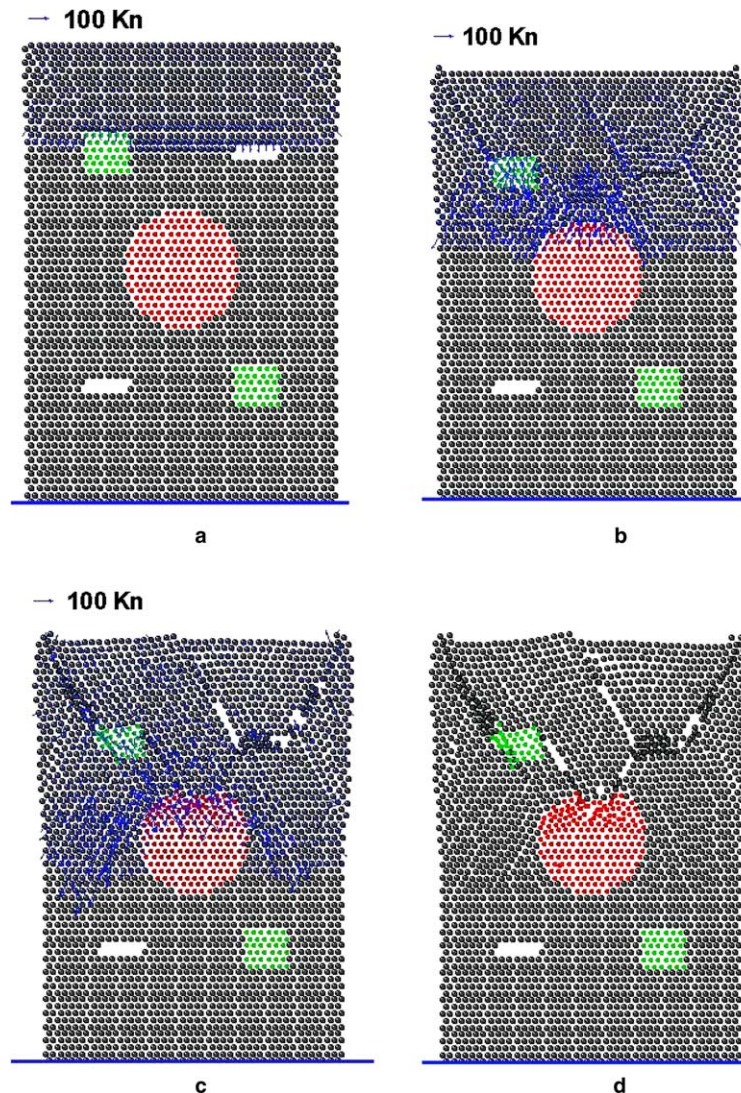


Fig. 11. A time sequence of crushing a composite material: (a) $T = 5.1 \times 10^{-6}$ s; (b) $T = 9.0 \times 10^{-6}$ s; (c) $T = 1.14 \times 10^{-5}$ s; (d) $T = 1.26 \times 10^{-5}$ s.

Fig. 5(b) shows the hexagon-shaped specimen (II) at 3.6×10^{-5} s. There are “^” crack lines accumulated inside the lower part of the specimen (II), formed from its center to the two lower ends. In Fig. 5(c), $T = 4.2 \times 10^{-5}$ s, we see the hexagon-shaped material is getting squashed, along the “^” crack lines, in height and extended horizontally. At this moment, the impact force at the top interface attains a high value. Finally, Fig. 5(d) shows the hexagon-shaped specimen being crushed at $T = 7.2 \times 10^{-5}$ s.

Fig. 6(b) shows the rectangular-shaped specimen (II) at 4.2×10^{-5} s. In a contradistinction to Fig. 5(b), the

“^” crack lines are now forming from the middle of the rectangular-shaped specimen’s top boundary toward its two corners at the bottom boundary. In Fig. 6(c), we see that, at $T = 6.4 \times 10^{-5}$ s, the mass of material (II) begins to slide along the “^” crack lines. Fig. 6(d) shows that the rectangular-shaped material is comminuted at $T = 8.4 \times 10^{-5}$ s.

Comparing the fracture patterns of two different blocks of the same material (II) in snapshots (d) of Figs. 5 and 6, we see that the rectangular-shaped specimen begins to crash at its top but the hexagon-shaped one at its lateral boundaries.

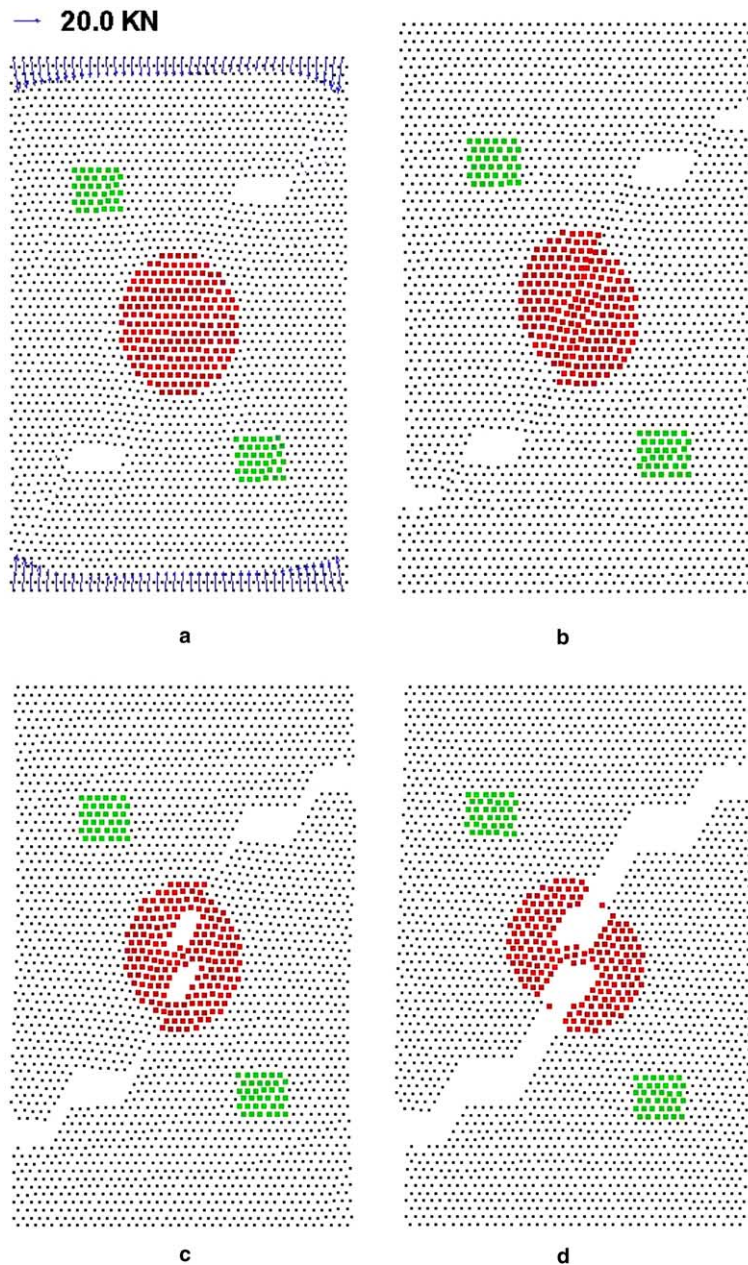


Fig. 12. Time-dependent results of stretching a composite material at 2.0 m/s both along the Y-axis: (a) $T = 1.24 \times 10^{-3}$ s; (b) $T = 1.28 \times 10^{-3}$ s; (c) $T = 1.32 \times 10^{-3}$ s; (d) $T = 1.36 \times 10^{-3}$ s.

The story is complemented by Figs. 7(a) and (b) and 8(a) and (b) showing the time-dependent force components of F_x and F_y recorded at the top and bottom points, respectively. In Fig. 7(a), we see that the horizontal force, F_x , is of a rather small amplitude, but characterized differently for these two different specimen shapes. Basically, in the case of the rectangular-shaped material, the comminution process causes less horizontal disturbance. By comparing Figs. 7(b) and 8(b), we find that the comminution of a rectangular-shaped block results in a larger reaction force F_y and needs more energy than that of the hexagonal-shaped one.

3.1.2. Fragmentation of a multi-phase material body

We now consider fragmentation processes of a composite three-phase specimen. Fig. 9 shows the matrix material body with inclusions (red and green) and two voids. The Lennard–Jones (p, q) parameters for all the phases are set up as follows:

matrix–matrix: $(p, q) = (7, 14)$

phase(I)–phase(I): $(p, q) = (3, 5)$

phase(II)–phase(II): $(p, q) = (5, 10)$

matrix–phase(I): $(p, q) = (2, 10)$

matrix–phase(II): $(p, q) = (2, 10)$

phase(I)–phase(II): $(p, q) = (2, 10)$

For simplicity, we assume that all the phases have the same mass density. The study is now conducted under a time-dependent loading prescribed via acceleration on the top boundary of the specimen (Fig. 10).

3.1.2.1. Crushing. Fig. 11(a) shows the displacement field at the instant $T = 5.1 \times 10^{-6}$ s when the disturbance only begins to reach the upper-defect (white void). We see that the force values are greatly decreased near the two upper

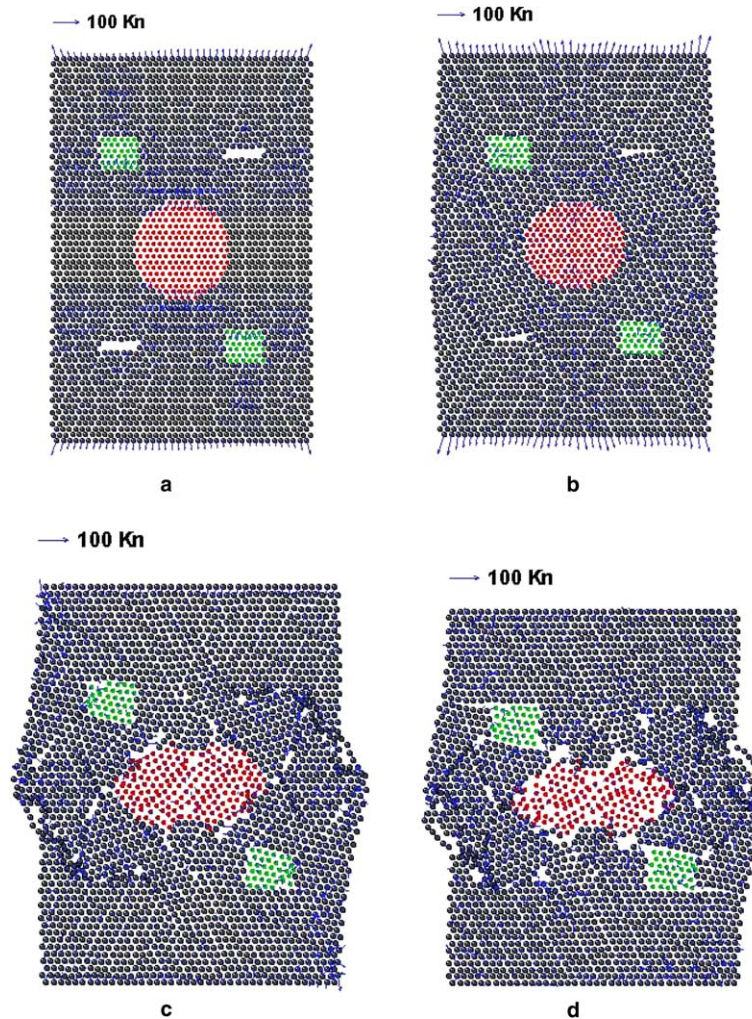


Fig. 13. Time-dependent results of composite material compression at 200 m/s along the Y -axis: (a) $T = 8.0 \times 10^{-6}$ s; (b) $T = 2.0 \times 10^{-5}$ s; (c) $T = 3.6 \times 10^{-5}$ s; (d) $T = 4.4 \times 10^{-5}$ s.

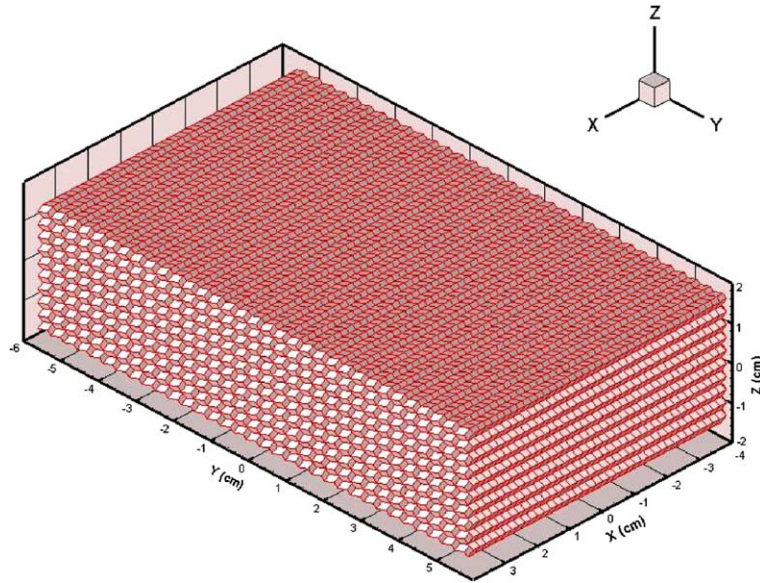


Fig. 14. A BCC-type meshing of a 3-D material body.

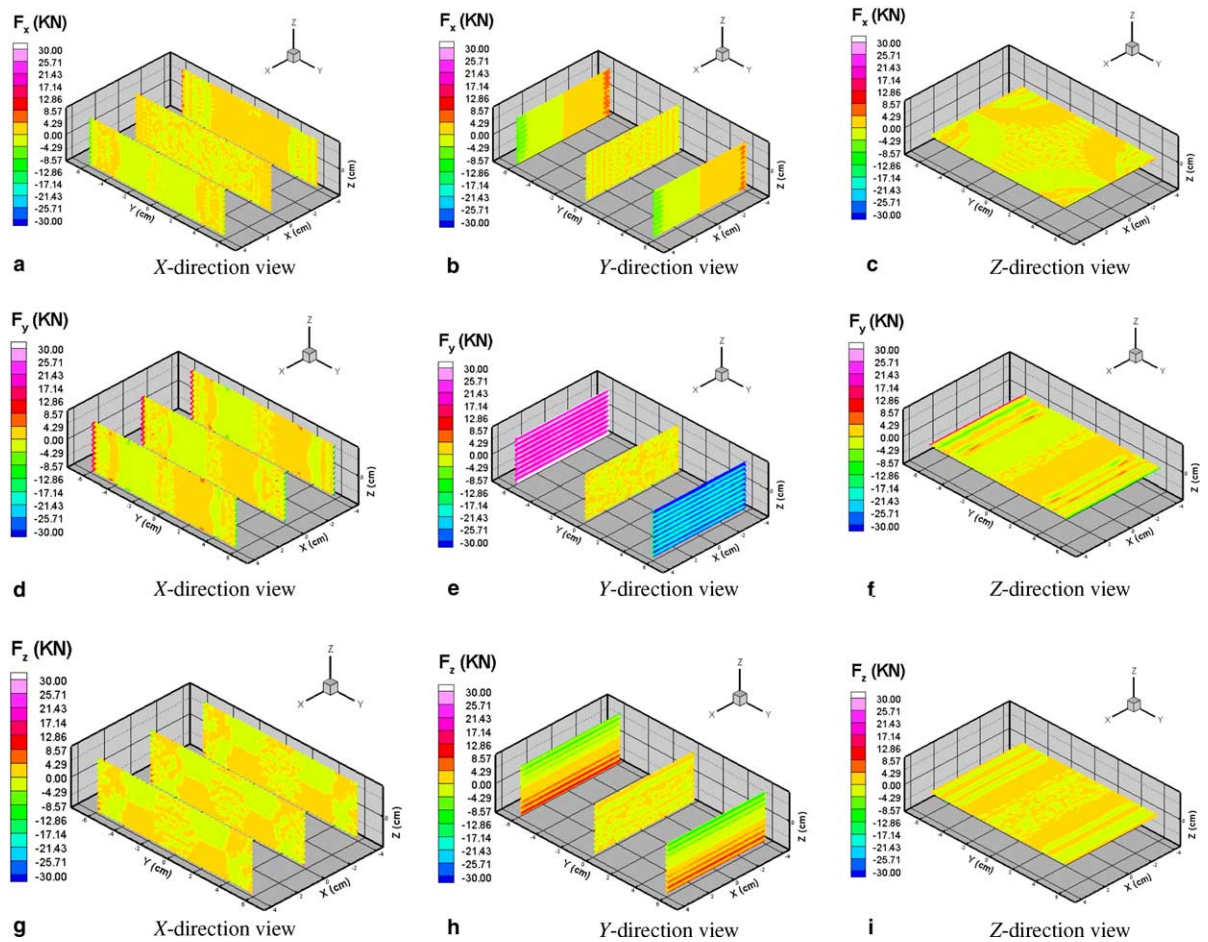


Fig. 15. Different directional views of force components in a 3-D body at stretching rate = 200 m/s along the Y-axis. (a)–(c): F_x ; (d)–(f): F_y ; (g)–(i): F_z , $T = 7.0 \times 10^{-5}$ s.

corners but stay nearly uniform at the remaining points of the top. Although both corners are less visibly extended horizontally, this already indicates there are lattice dislocations occurring there. With the time marching forward, at the instant $T = 9.0 \times 10^{-6}$ s shown in Fig. 11(b), the top defect disappears altogether due to the impact. Material (I) is squashed a little on its top, while material (II) is distorted. The onset of cracks can be discerned in the top region. Fig. 11(c) and (d) show further evolution of cracks at $T = 1.14 \times 10^{-5}$ s and $T = 1.26 \times 10^{-5}$ s, respectively. From these two snapshots we see that, with the cracks now penetrating across the composite, the top part of the specimen is finally broken into four clearly distinguishable pieces. Fig. 11(c) also shows that damage propagates faster in the hard matrix material than in the soft phase (I).

3.1.2.2. Extension. Initial conditions: The stretching rate is $v = 2.0$ m/s and $u = v = 0.0$ m/s for the remainder of particles at $T = 0.0$ s. ΔT is determined by the method discussed in [1].

Boundary conditions: Traction-free conditions are set on the other boundaries except that the top and bottom are at constant kinetic condition of $v = 2.0$ m/s.

Fig. 12(a)–(d) show the time sequence of fragmentation. First, Fig. 12(a) shows the force distribution on the top boundary. Next Fig. 12(b) indicates that a diagonal shear band is formed inside the matrix and phase (I) at $T = 1.28 \times 10^{-3}$ s. Fig. 12(b)–(d) show snapshots of fracture evolution developing from the initial shear band. In particular, (b) shows that, at $T = 1.28 \times 10^{-3}$ s, cracks appear on the lateral boundaries near the voids (or defects) and phase (I) is being distorted further. These cracks then propagate diagonally into the voids, at $T = 1.32 \times 10^{-3}$ s in Fig. 12(c). Finally, at $T = 1.36 \times 10^{-3}$ s in Fig. 12(d), a complete fracture pattern is caused that shears the composite (I).

3.1.2.3. Compression. Contrary to the above example, in this case, the top and bottom are compressed inward at a constant velocity of 200 m/s. ΔT is determined by the method discussed in [1].

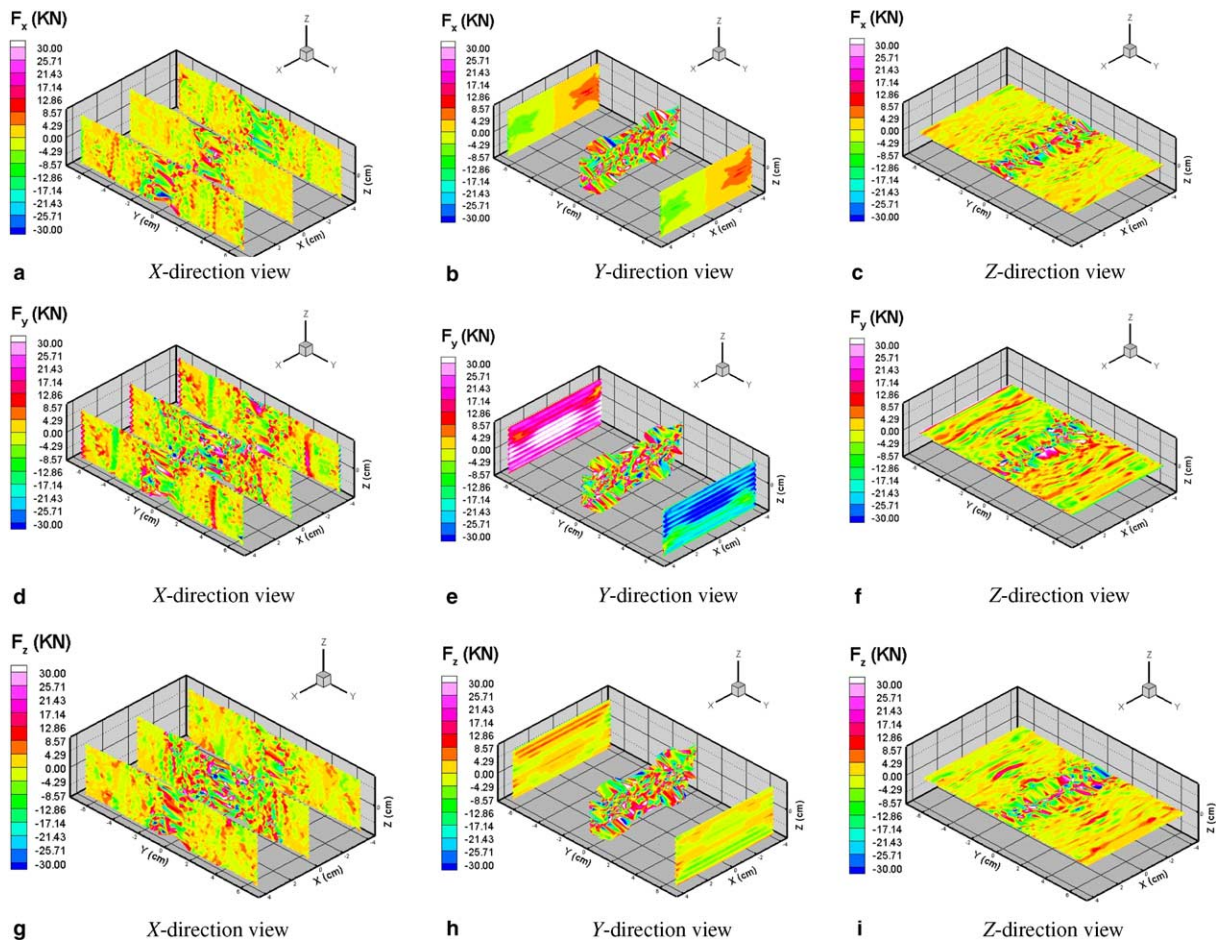


Fig. 16. Different directional views of force components in a 3-D body at stretching rate = 200 m/s along the Y-axis. (a)–(c): F_x ; (d)–(f): F_y ; (g)–(i): F_z , $T = 4.7 \times 10^{-4}$ s.

Fig. 13(a) shows the vector results at $T = 8.0 \times 10^{-6}$ s, from which we can see how the reaction force is being transmitted and distributed within different phases. At $T = 2.0 \times 10^{-5}$ s, shown in Fig. 13(b), the whole body is compressed vertically by this impact, with the middle part being extended laterally. Some cracks can be discerned near the defects. Fig. 13(c) shows that, at $T = 3.6 \times 10^{-5}$ s, the fragmentation occurs mainly horizontally in the middle part of the body, and phase (I) is split vertically in the middle. Fig. 13(d) shows a

further state at $T = 4.4 \times 10^{-5}$ s when more fragments appear at the composite material interfaces. We can also clearly see that the interface between phase (I) and the matrix becomes debonded.

3.2. Fragmentation of a 3-D single-phase material body

Stretching and compression of a 3-D single-phase material body are studied in this section. A BCC-type 3-D meshing system shown in Fig. 14 is used for

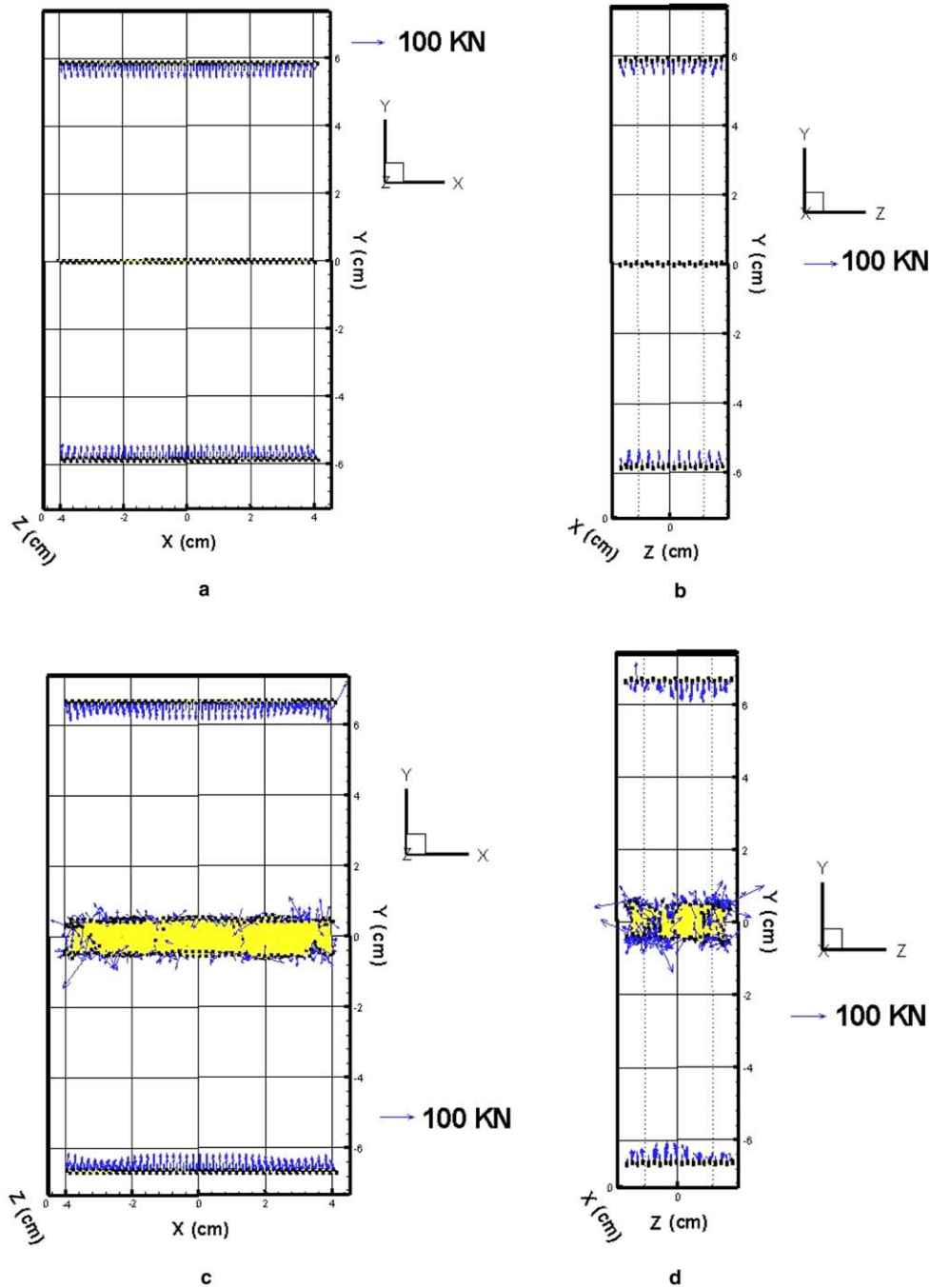


Fig. 17. Different planar views of total force distribution in a 3-D body at stretching rate = 200 m/s along the Y-axis. (1) at $T = 7 \times 10^{-5}$ s: (a) XY-plane, (b) YZ-plane; (2) at $T = 4.7 \times 10^{-4}$ s: (c) XY-plane, (d) YZ-plane.

simulations with $(p, q) = (7, 14)$. Here we choose one mid- and two surface-planes along X - and Y -axes and one middle XY -plane in Z -axis to show the time-dependent force distributions.

3.2.1. Extension

The kinematical boundary conditions are set up as follows: the two surfaces along the Y -axis are both stretched outward at a constant speed of 200 m/s and the remainder of the boundary is traction-free. The initial condition inside the body is zero-velocity at $T = 0.0$ s. ΔT is determined by the method discussed in [1].

Fig. 15(a)–(i) shows the distributions of F_x , F_y and F_z from different coordinate points of view at $T = 7.0 \times 10^{-5}$ s when no fracture happens. From plots of F_x and F_z , in Fig. 15(a)–(c) and Fig. 15(g)–(i), we find that mid-sections in all these figures are not affected by this

stretching yet, with nearly zero-averaged force value. From Fig. 15(b) and (h) we see that, the distributions of F_x and F_z on all the boundaries are obviously higher in magnitude than in the interior. This shows the effect of a dynamic constraint that gradually propagates from the boundaries inward. Fig. 15(d)–(f) shows the F_y distributions in three orthogonal planes of X -, Y - and Z -axes, respectively. Fig. 15(e) demonstrates that the two edges in Y -direction are being pulled apart with high force amplitude but display a very small force in the mid-section at that instant.

Fig. 16(a)–(i) shows the distribution of force components of F_x , F_y and F_z from different coordinate points of view at $T = 4.7 \times 10^{-4}$ s when fracture takes place. The similarities among these figures are that the high force concentration exists where fracture occurs no matter F_x , F_y or F_z is plotted. The fracture is located mainly in the middle of the material body along the stretching

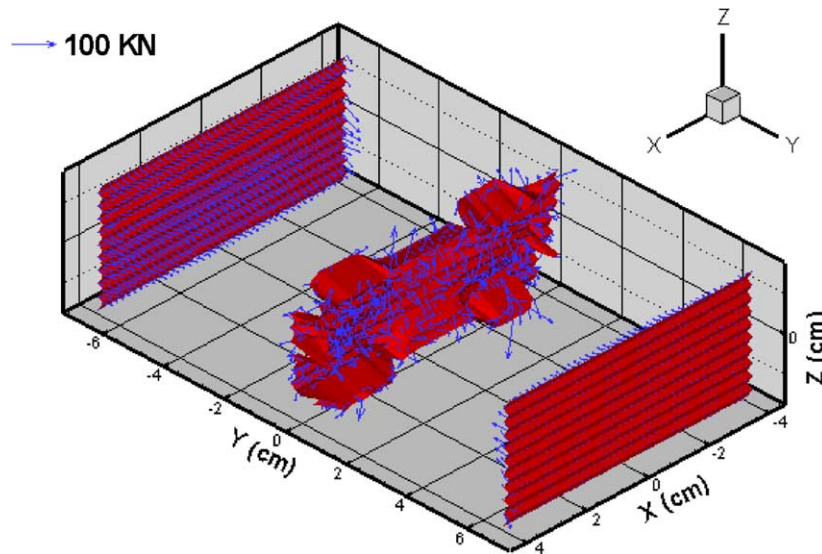


Fig. 18. Total force distribution of a 3-D body at stretching rate = 200 m/s along the Y -axis, $T = 4.7 \times 10^{-4}$ s.

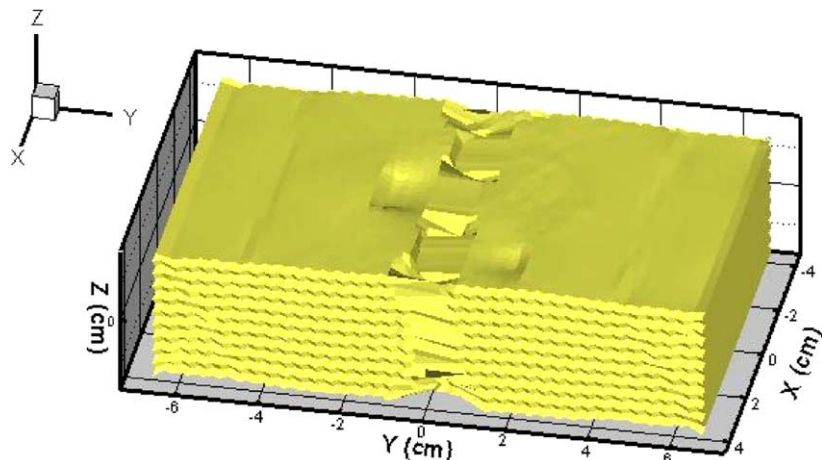


Fig. 19. Fracture of a 3-D body at stretching rate = 200 m/s along the Y -axis, $T = 4.7 \times 10^{-4}$ s.

direction, causing the original mid-flat-plane to be twisted. Fig. 16(b), (e), and (h) also show that the fracture inside the body greatly affects the loadings at both ends in the Y-direction.

Fig. 17(a) and (b) give the XY- and YZ-plane cross sections of the total force distributions at three plane-sections along the Y-axis at time of $T = 7 \times 10^{-5}$ s and Fig. 17(c) and (d) at time $T = 4.7 \times 10^{-4}$ s. From the first two pictures we see that the force is fairly uniformly distributed at the two edges with almost zero-value at the mid-plane. From the last two pictures—fracture taking place—we clearly see how the fracture occurs the mid-plane. The fracture inside the material due to this stretching changes the loading on the two edges.

Fig. 18 shows the total force distributions on three XZ-planes along the Y-axis in a 3-D view at 4.7×10^{-4} s. It is clearly seen that high force magnitudes occur wherever the fracture does and, consequently, they change the loading on the both ends along the Y-axis.

Fig. 19 provides a snapshot 3-D view of fracture at $T = 4.7 \times 10^{-4}$ s. We clearly see that fracture occurs mainly in the mid-part of the body along the direction of stretching.

3.2.2. Compression process

The kinematic boundary conditions are set as follows: the two surfaces along the Y-axis are both compressed inward at a constant speed of 200 m/s while the remaining ones are traction-free. The initial condition throughout the body is zero-velocity at $T = 0.0$ s. ΔT is determined by the method discussed in [1].

Fig. 20(a)–(i) shows the distributions of force components of F_x , F_y and F_z from different coordinate points of view at $T = 6.0 \times 10^{-6}$ s when no fracture occurs. We find that all the mid-sections in that figure are not yet affected by compression at this instant. Comparing Fig. 20(a) and (b) with Fig. 20(g) and (h), we find that F_x has a larger value on the lateral surfaces than F_z does.

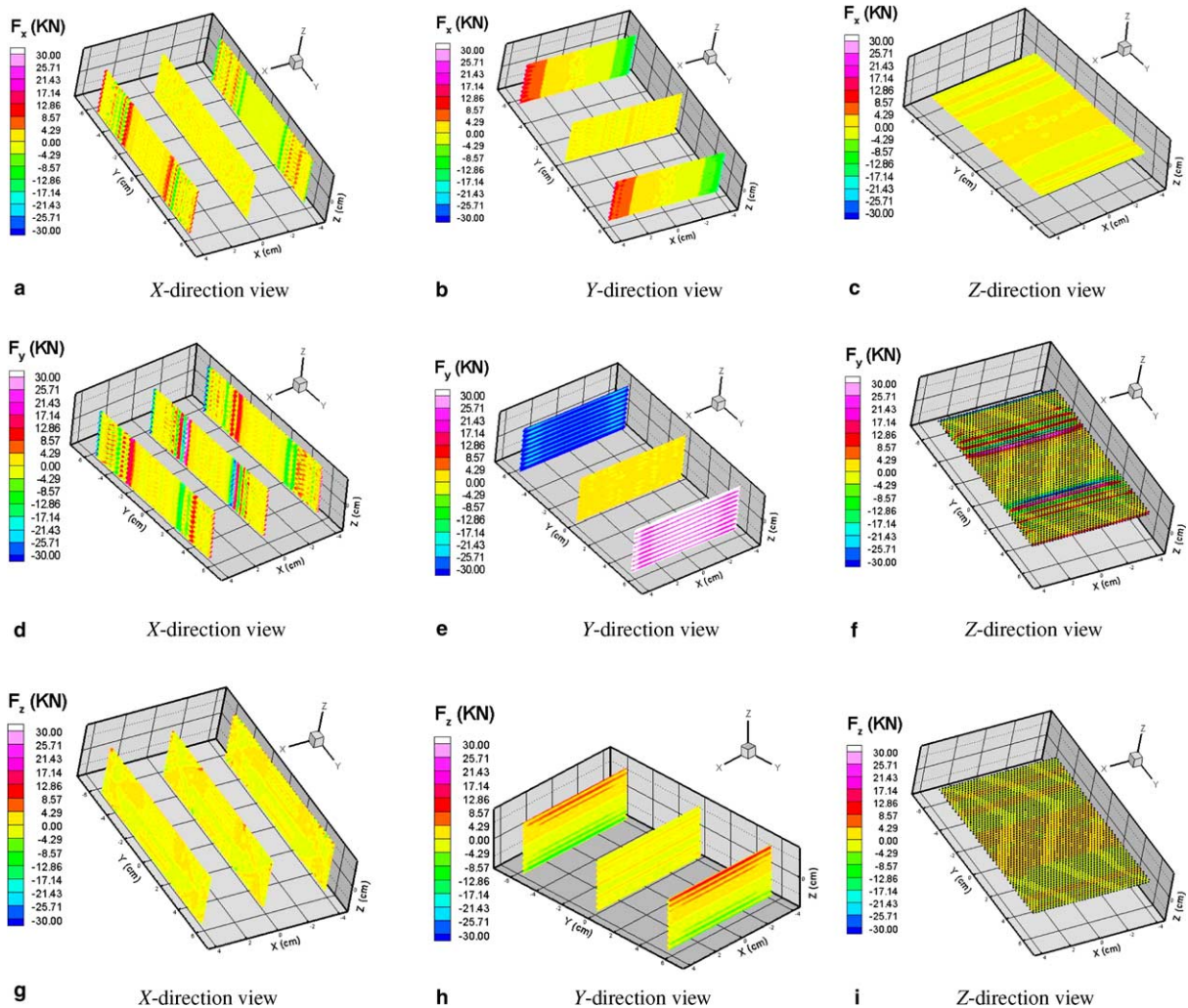


Fig. 20. Different directional points of view of force components in a 3-D body at compression rate = 200 m/s along the Y-axis. (a)–(c): F_x ; (d)–(f): F_y ; (g)–(i): F_z ; $T = 6.0 \times 10^{-6}$ s.

The reason is that this compression results in much greater expansion along the X -axis than the Z -axis—this is also illustrated in Fig. 22. From these figures, we can also see the force transfer trajectories. Fig. 20(d) and (f) shows the F_y distributions in different planes, whereby the loading propagating from boundaries toward the mid-section is captured. Fig. 20(e) shows that the two edges along the Y -axis are compressed with a high force, but this compression hardly affects the mid-section at the particular moment.

Fig. 21(a)–(i) show the distributions of force components of F_x , F_y and F_z from different coordinate points of view at $T = 3.3 \times 10^{-5}$ s when fracture occurs. Observing high force concentration distributed in Fig. 21(b) and (e), we conclude that fracture takes place at four corners of the body. From Fig. 21(c), (f), and (i), a clear “X”-shape crack is shown on the XY -plane. Also, fracture occurs in the central part of the body.

The geometry change on the lateral boundaries in Fig. 21(a), (d), and (g) reveals that a drum-like expansion results from this compression.

Fig. 22(a) and (b) gives the XY - and YZ -planar points of view to the total force distributions at three plan-sections along Y -axis at $T = 3.3 \times 10^{-5}$ s. As has been discussed above, the compression causes a greater expansion in the X -direction than in the Z -direction. Thus, Fig. 22 explains again why much smaller value of F_z than F_x are shown. Fig. 22(a) shows that fracture happens at the four corners in the plane where high force concentration is shown. Meanwhile, the central part of the mid-section is torn out and this then reduces the loading on the top- and bottom boundaries.

Fig. 23 displays the total force distributions on three XZ -planes along the Y -axis in a 3-D view at time 3.3×10^{-5} s. It is clearly seen again that high force

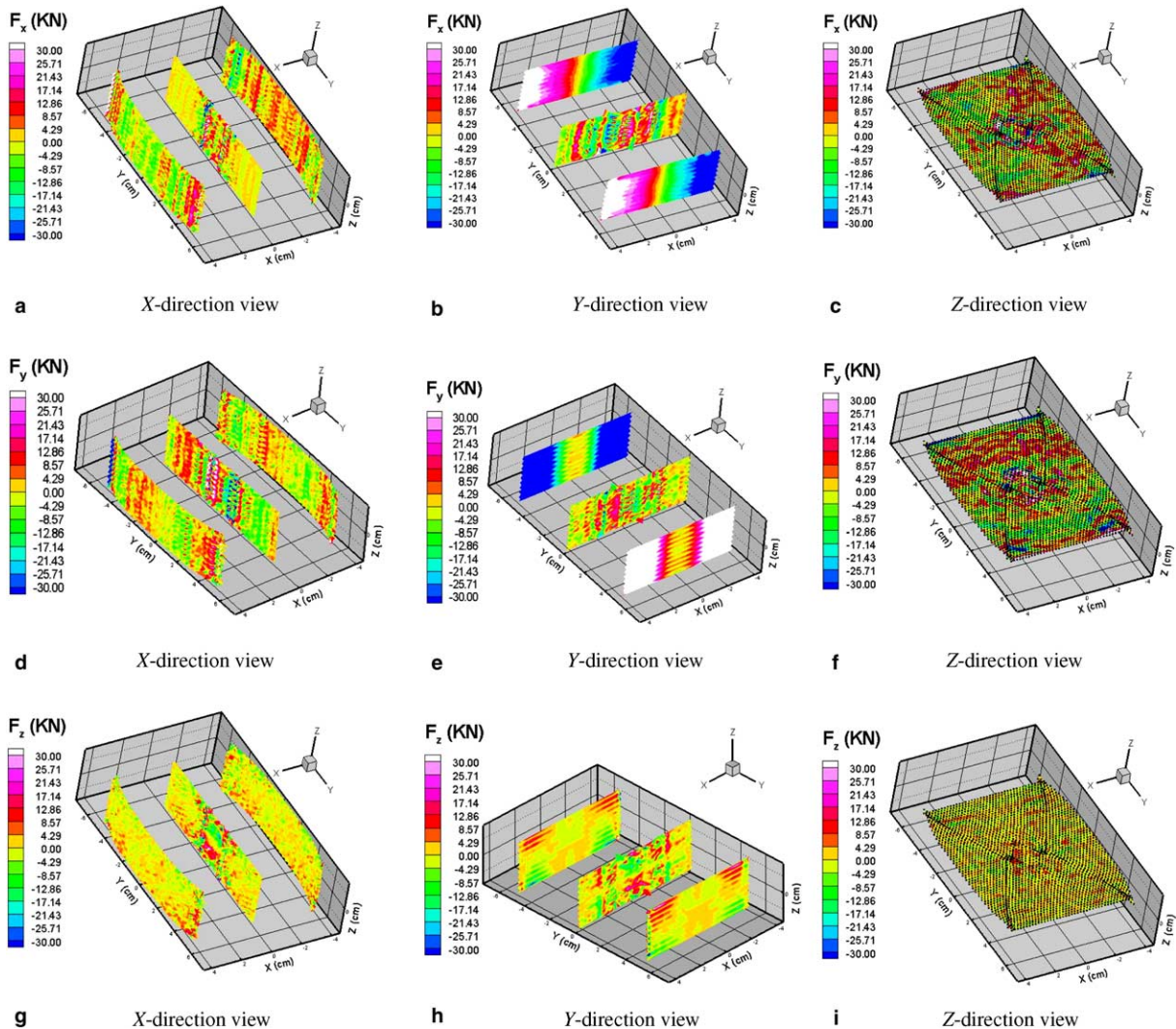


Fig. 21. Different directional points of view to force components of a 3-D body at compression rate = 200 m/s along the Y -axis. (a)–(c): F_x , (d)–(f): F_y , (g)–(i): F_z , $T = 3.3 \times 10^{-5}$ s.

amplitudes due to the fracture, occurring in the central part of the body, reduce the loading on both ends in the Y-direction. It is also seen that fracture initiates from four corners of the body.

Fig. 24 shows a 3-D point of view of surface fracture at $T = 3.3 \times 10^{-5}$ s. We clearly see that an X-shaped crack diagonally connects four corners through the material body. Also, fracture occurs in the central part of

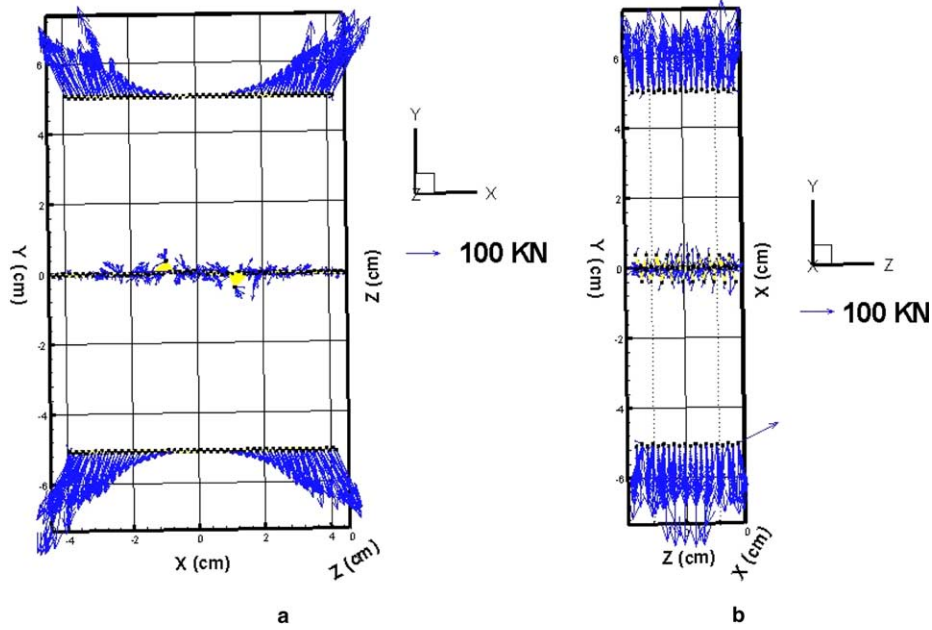


Fig. 22. Different planar point of view to total force distribution of a 3-D body at compression rate = 200 m/s along the Y-axis. $T = 3.3 \times 10^{-5}$ s: (a) XY-plane, (b) YZ-plane.

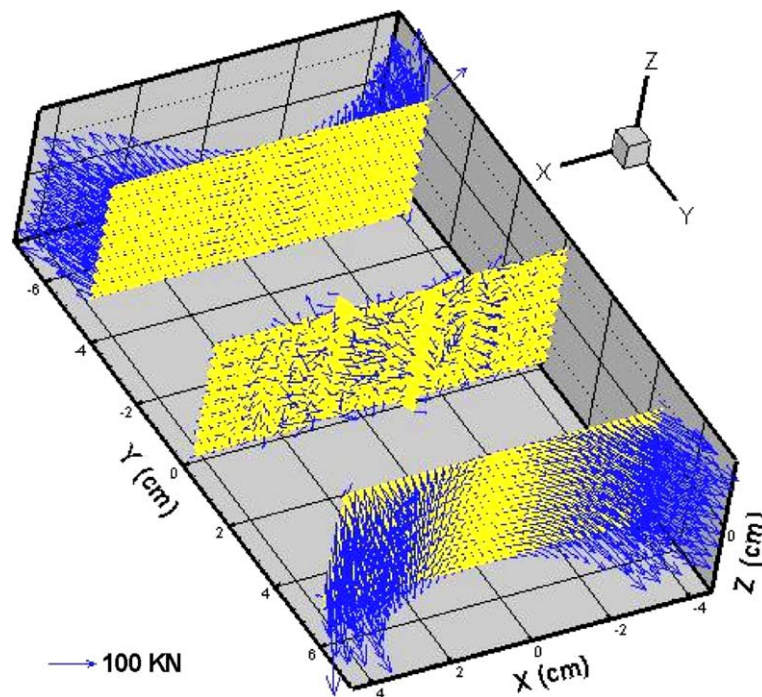


Fig. 23. Total force distribution of a 3-D body at compression rate = 200 m/s along the Y-axis, $T = 3.3 \times 10^{-5}$ s.

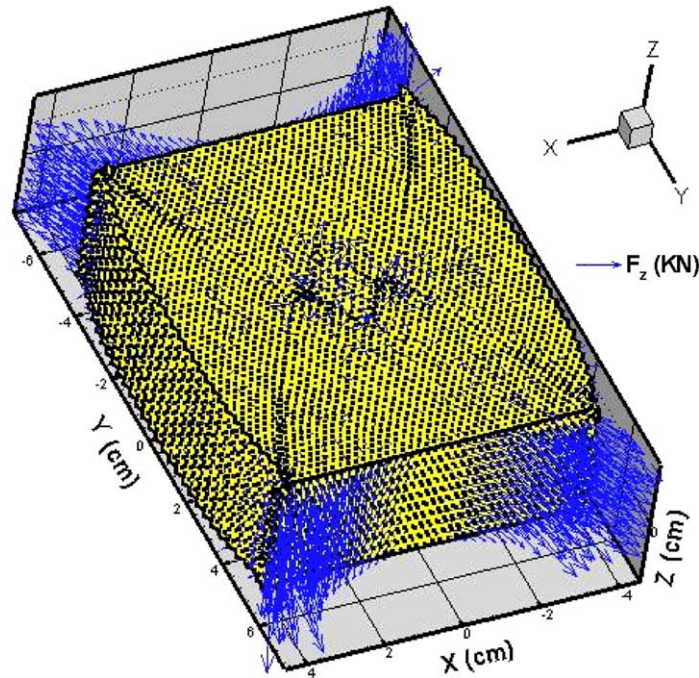


Fig. 24. Fracture of a homogeneous 3-D body at compression rate = 200 m/s along the Y -axis, $T = 3.3 \times 10^{-5}$ s.

of the body, and the force vector shows that it reduces the compressive loading.

4. Conclusions

In this paper we apply particle modeling (PM) to simulate several typical cases in dynamic fragmentation of 2-D and 3-D materials. We simulate single- and multi-phase materials under compressive or stretching loadings, corresponding to various comminution and blasting processes. These simulations show patterns and trends of fragmentation of materials in function of their constitutive properties, their geometric shapes, and the loading conditions. Our ongoing research work is focused on comparisons of PM simulations with corresponding experimental tests on specimens of nominally identical geometries and compositions. A paradigm of such a comparison was given in the context of planar elastic-brittle polycrystals in static loading [9].

Let us close this paper with an observation that, just like a partition of the material domain into finite elements (FE), the PM discretization into quasi-particles is also somewhat artificial. At the same time, it is worthwhile noting some key advantages of PM vis-à-vis FE:

- (i) the ease to account for the constitutive behavior of the same (functionally very non-linear and asymmetric) type as on the molecular level: response in compression being qualitatively different from that in tension;

- (ii) the ease to effect fracture (or re-bonding) of the lattice by disconnecting (or connecting) contiguous quasi-particles;
- (iii) the mathematical simplicity of the PM for physically and geometrically non-linear systems, in contradistinction to the mathematical complexity of FE schemes whenever any non-linearity needs to be accounted for.

The PM is not free of limitations. The key challenges requiring new work are:

- (i) setting up an interaction potential—such as that of Lennard–Jones type—for arbitrary elastic material properties; the method developed in [1] does not cover all the possibilities, although it covers rocks very well;
- (ii) setting up an interaction potential for inelastic and rate-dependent materials;
- (iii) experimental validation of PM, currently underway, involving a comparison of PM simulations with laboratory tests, such as conducted in the test of Fig. 3.

Acknowledgements

We have benefited from correspondence with Prof. D. Greenspan (University of Texas at Arlington). The work reported herein has been supported by the Canada Research Chairs program, NSERC, and COREM.

References

- [1] G. Wang, M. Ostoj-Starzewski, Particle modeling of dynamic fragmentation—I: Theoretical considerations, *Comput. Mater. Sci.* 33 (4) (2005) 429–442.
- [2] D. Greenspan, *Computer-Oriented Mathematical Physics*, Pergamon press, 1981.
- [3] D. Greenspan, Supercomputer simulation of cracks and fractures by quasi-molecular dynamics, *J. Phys. Chem. Solids* 50 (10) (1989) 1245–1249.
- [4] D. Greenspan, *Particle Modeling*, Birkhäuser Publishing, 1997.
- [5] D. Greenspan, New approaches and new applications for computer simulation of N-body problems, *Acta Appl. Math.* 71 (2002) 279–313.
- [6] H. Kitagawa, Challenge to mesoscopic dynamics of fracture, *Mesoscopic Dynamics of Fracture—Computational Material Design*, Springer Verlag, 1998, pp. 2–11.
- [7] R.W. Smith, Computer simulation of intergranular stress corrosion cracking via hydrogen embrittlement, *Model. Simul. Mater. Sci. Eng.* 8 (2000) 629–648.
- [8] A.V. Potapov, C.S. Campbell, The breakage induced by a single ball dropped onto a randomly packed particle bed, *Powder Technol.* 107 (2000) 108–117.
- [9] M. Grah, K. Alzebdeh, P.Y. Sheng, M.D. Vaudin, K.J. Bowman, M. Ostoj-Starzewski, Brittle intergranular failure in 2D microstructures: experiments and computer simulations, *Acta Mater.* 44 (10) (1996) 4003–4018.